inter·noise 2023
CHIBA,GREATER TOKYO 20-23 AUGUST

Practical tutorial on cylindrical structure vibro-acoustics Part 2 – Acoustics

Stephen A. Hambric[1]
Hambric Acoustics, LLC

ABSTRACT

In part 1 of this tutorial (proceedings of Inter-noise 2022) I explained vibrations in cylindrical shell structures. In that paper I limited the mathematics and focused on the key behavior of shells based on critical parameters like the ring frequency, helical wavenumbers, and mean mobilities over different frequency ranges. I compared measured data to the simple theories. In part 2, I focus on the acoustics of cylindrical shells, including sound within shells and the sound radiated outside them. Exterior sound radiation depends strongly on the circumferential order of the shell modes. Breathing modes near the ring frequency radiate sound extremely well, but have very high impedances, so can be difficult to excite. Beam-like modes, where the entire shell cross-section vibrates transversely, radiate less efficiently, but can be easily driven. Higher order, or 'lobar' modes radiate even less efficiently, but nevertheless are commonly observed in radiated sound spectra due to their low impedances. I also review statistical estimates of radiation efficiency of groups of shell modes, which show clear peaks at both the ring frequency as well as at the critical frequency of bending waves. The mathematics of sound inside cylindrical shells is some of the most challenging in vibro-acoustics. At low frequencies, however, the interior sound is dominated by simple one-dimensional planar acoustic waves. At higher frequencies, the sound depends on how well a shell vibration field matches the interior acoustic field based on proximity of resonance frequencies and the similarity of mode shape orders, as well as the 'cut on' frequencies of higher order internal acoustic modes. Finally, I review the well-known phenomenon of how a low shell wall impedance can reduce the effective acoustic sound speed of one-dimensional waves inside cylindrical shells.

1. INTRODUCTION

In part 1 of this tutorial [1] I reviewed cylindrical shell vibration theory. Perhaps the most important shell parameter is the *ring frequency*, at which the in-plane structural wavelength matches the shell circumference:

$$f_r = \frac{c_p}{2\pi a}$$

where

$$c_p = \sqrt{\frac{E}{(1-\upsilon^2)\rho_s}}$$

and E is Young's Modulus, ν is Poisson's ratio, and ρ_s is structural mass density.

[1] hambricacoustics@gmail.com, www.hambricaocustics.com

Frequency is commonly normalized by the ring frequency as:

$$\Omega = \frac{f}{f_{ring}} = \frac{\omega}{\omega_{ring}}.$$

I also showed in part 1 that the normalized frequency Ω is useful for subdividing frequency ranges where shells behave as simple beams (low frequencies), curved shells, and infinite flat panels (high frequencies). I encourage you to read Part 1 before this paper.

In Part 2 I will explain, once again with minimal mathematics, how acoustic regions outside and inside cylindrical shells couple to shell vibrations. You will learn about which types of shell modes radiate sound the most efficiently, how at low frequencies the sound inside shells is due to simple one-dimensional acoustic waves, and finally how flexible shell walls can reduce the effective acoustic sound speeds.

2. EXTERIOR SOUND RADIATION

Along with the ring frequency, the other important parameter related to exterior sound radiation is *critical frequency*[2], which is defined for shells the same way it is for flat panels: as the frequency where acoustic and structural flexural waves have the same speeds:

$$f_c = \frac{c_0^2}{2\pi}\sqrt{\frac{\rho_s h}{D}}$$

where c_0 is the acoustic sound speed, h is the shell thickness, and the flexural rigidity is

$$D = \frac{E h^3}{12(1-\upsilon^2)}.$$

Exterior radiated sound is strongest at and around the ring and coincidence frequencies and has a constant unit radiation efficiency above f_c. Let's examine first how individual modes radiate sound, and later a statistical average of radiation efficiency over groups of modes.

2.1. Mode Order Dependence

Each individual mode radiates sound differently depending on how well it couples with a surrounding acoustic region. For shells, we denote mode orders by their circumferential harmonics n, and axial harmonics m (see Figure 5 of Part 1 for some example mode shapes). The circumferential harmonic n is the most important for sound radiation effectiveness. Figure 1 shows simplified low-frequency radiation efficiency trends for the lowest three circumferential harmonics (at high frequencies, above coincidence, all modes radiate equally well).

Breathing modes, where $n = 0$, radiate like monopoles since the entire shell circumference vibrates in phase against the acoustic region. Breathing mode frequencies tend to cluster around the ring frequency (see Figure 6 in part 1). The entire cross section vibrates transversely at $n = 1$ modes, which are *beam-like*. These radiate sound like dipoles, which are less efficient than breathing modes. The lowest order *lobar* modes are $n = 2$, where the cross-section ovalizes. These resemble quadrupole radiators, which are even less efficient. Higher lobar mode harmonics (n =3, 4, 5, …) radiate even less efficiently below coincidence.

[2] Sometimes called the coincidence frequency.

Although breathing modes radiate more efficiently than beam modes, which radiate more efficiently than lobar modes, the actual radiated sound power from these mode types also depends on how well they may be driven by a structural load. This depends on the structural mobilities (transverse vibration velocity due to a specific applied force). Breathing mode mobilities are generally quite low due to their very high stiffness (this also leads to very high resonance frequencies). Beam mode mobilities are much higher, as they depend on the length-wise stiffness of a shell. Lobar mode mobilities are even higher. Therefore, although lobar modes may not radiate sound efficiently, they still radiate audible sound levels since they are easy to drive. We'll examine an example of this next.

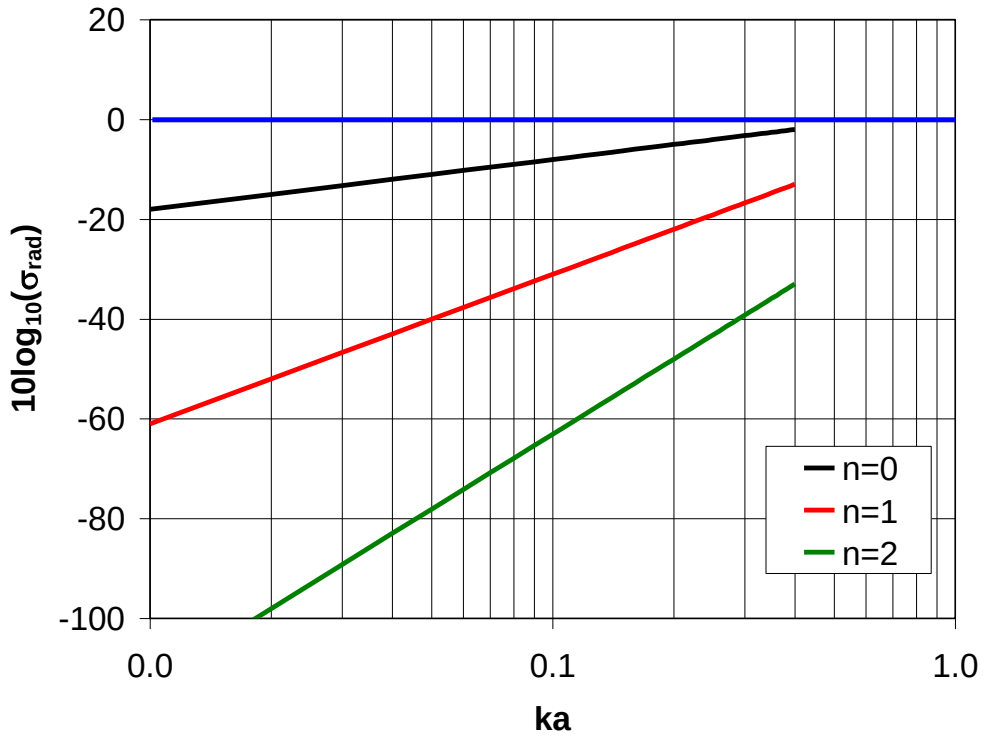

Figure 1: Approximate low-frequency (*ka*) sound radiation frequency dependencies of breathing modes ($n = 0$), beamlike bending modes ($n = 1$), and lobar modes ($n = 2$ and higher).

Examples of several measured sound power transfer functions (Power/Force^2) for an elbowed pipe submerged in water (defined in Figure 2 of Part 1) are compared in Figure 2 to the sound power radiated by a point dipole source[3]:

$$\frac{P_{rad}}{F^2} = \left(\frac{1}{12\pi}\right)\left(\frac{1}{\rho_0 c_0}\right)k_0^2$$

We consider sound radiation greater than that from a point dipole to be amplified by the pipe. In a pipe with a small radius, the ring frequency (and therefore the breathing mode frequencies) is very high, and above the range of the frequencies measured. The lowest frequency peaks are due to pipe bending ($n = 1$), followed by $n = 2$ modes and then $n = 3$ modes. This progression of modal harmonics over frequency is typical of small radius shells, or pipes. Note the strong radiation by the $n = 2$ modes is due mainly to the high mobility of those modes. The $n = 3$ modes are also audible, although less strong than the $n = 2$ modes due to their lower radiation efficiency.

[3] These sound powers were measured in a reverberant tank of water and are therefore limited to one-third octave frequency bands.

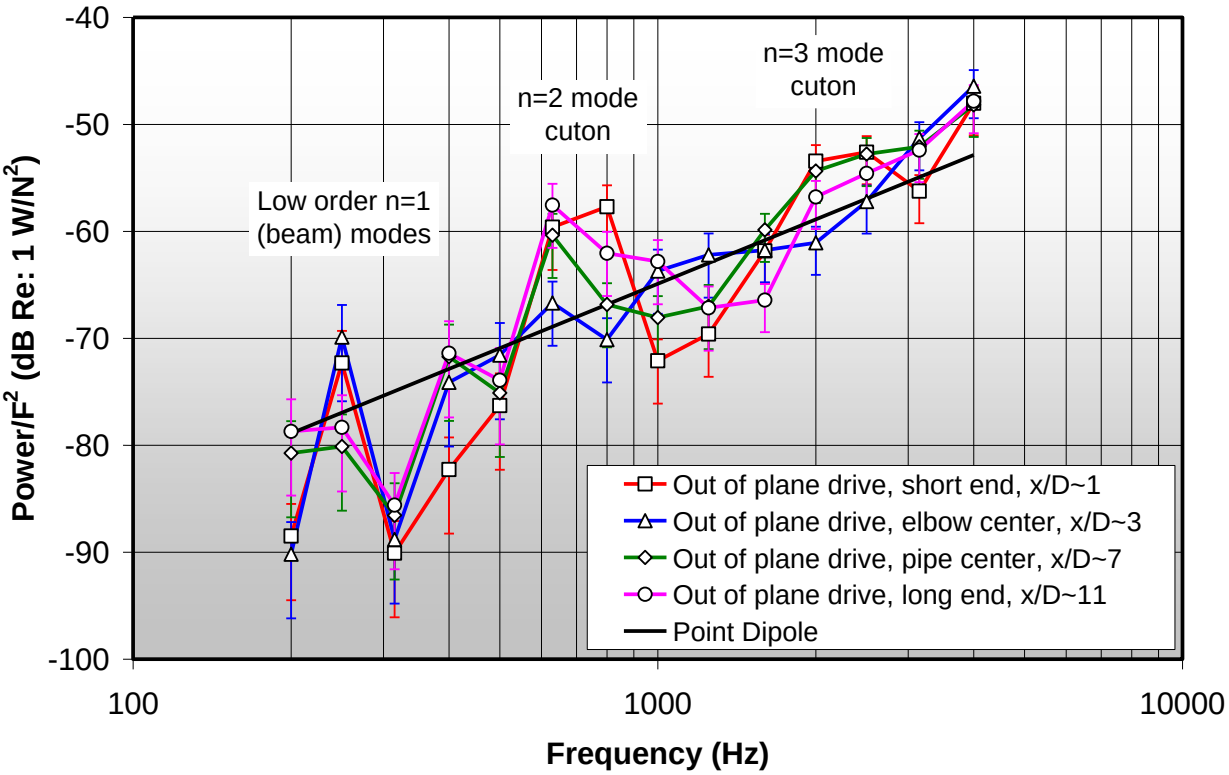

Figure 2: Measured sound power transfer functions from a transversely driven elbowed pipe submerged in water [2] compared to sound radiated from a point dipole source.

Figure 3 shows the the analytically calculated sound pressure radiated from Junger and Feit's [3] submerged cylindrical shell example. Here, the radius is much larger, and the ring frequency is within the frequency range of the calculations (at a *ka* slightly higher than 1). Many other mode orders are also present, as denoted at the peaks in the radiated pressure shown in the bottom plot. Junger and Feit normalize frequency to non-dimensional wavenumber *ka*, where *k* is the acoustic wavenumber ω / c_0 and *a* is the shell radius. A *ka* of π indicates a half acoustic wavelength spans the dimension *a*. The pressure is calculated in the acoustic far-field, normal to the shell surface, in line with the applied input force, and is also normalized, this time by two physical dimensions (*a* and radial distance *R*) and the input force *F*.

Calculations are shown in the plot for two length to radius aspect ratios: $L / a = 1$ and $L / a = 2$. The calculations are compared to the sound pressure radiated by another point dipole (denoted infinite plate in the plot). Once again, sound greater than that from a point dipole is considered to be amplified by the shell. At low frequencies ($ka < \pi$), the shell vibrations are dominated by stiff in-plane membrane behavior and the radiation is strong. As frequency increases, the shell vibrations become more like those in an infinite flat panel and dominated by transverse flexure, and the sound radiates like that of an infinite panel. The bottom plot in Figure 3 denotes the peaks with their corresponding mode orders. As expected at low frequencies, the strongest radiating modes are of low order (breathing, beam-like, ovalling).

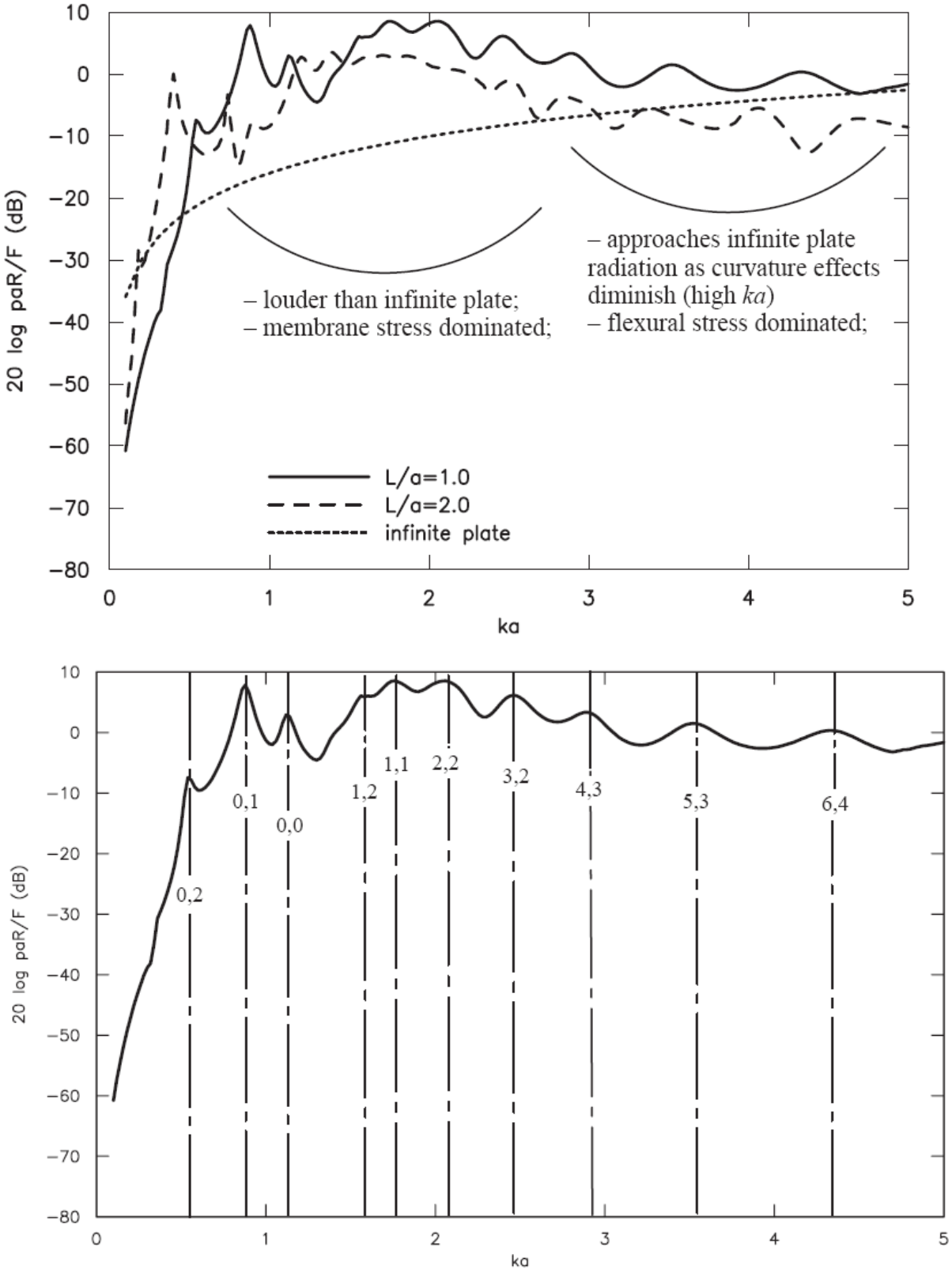

Figure 3: Simulated far-field radiated sound pressures (normalized by shell radius, far-field location r, and input force) normal to the shell surface induced by a point drive at the shell center. Frequency is normalized to ka. After Junger and Feit [3]. Top: sound pressure transfer functions for shells with two L/a ratios. Bottom: annotation of the $L/a = 1$ sound pressure to denote dominant radiating modes (m, n).

Figure 4 shows the near-field acoustic intensity measured over a cylindrical surface surrounding another submerged cylindrical shell [4] attached to solid hemispherical end caps. Acoustic intensity is sound power over a small area and denotes the outwardly propagating sound, measured at a given frequency as:

$$I = \frac{1}{2} Re(pv^*)$$

where p is pressure and v is particle velocity. The pressure and particle velocity is measured simultaneously with an underwater acoustic intensity probe [5] in the near-field of the shell.[4]

The intensity distribution is mapped over circumferential angle (the x-axis) and height (the y-axis). The shell geometry is shown between the two intensity plots, along with the location of an internal shaker used to generate a point force. The *raw* intensity (left plot) shows a dominant modal pattern of $n = 2$ around the circumference and $m = 3$ along the length. Transforming the acoustic pressure and particle velocity into wavenumber space in both the axial and circumferential directions, and then limiting the acoustic intensity calculation to supersonic wavenumbers ($k < k_0$) and finally, inverse-transforming back to spatial coordinates yields the *supersonic acoustic intensity* shown in the plot on the right side of the figure. This approach filters out high-order subsonic modes (where the modal wavenumber is larger than the acoustic wavenumber). Now, the dominant radiating mode is clearly revealed as $n = 0$, $m = 1$. Once again, it is the low-order modes that radiate the most sound at low frequencies.

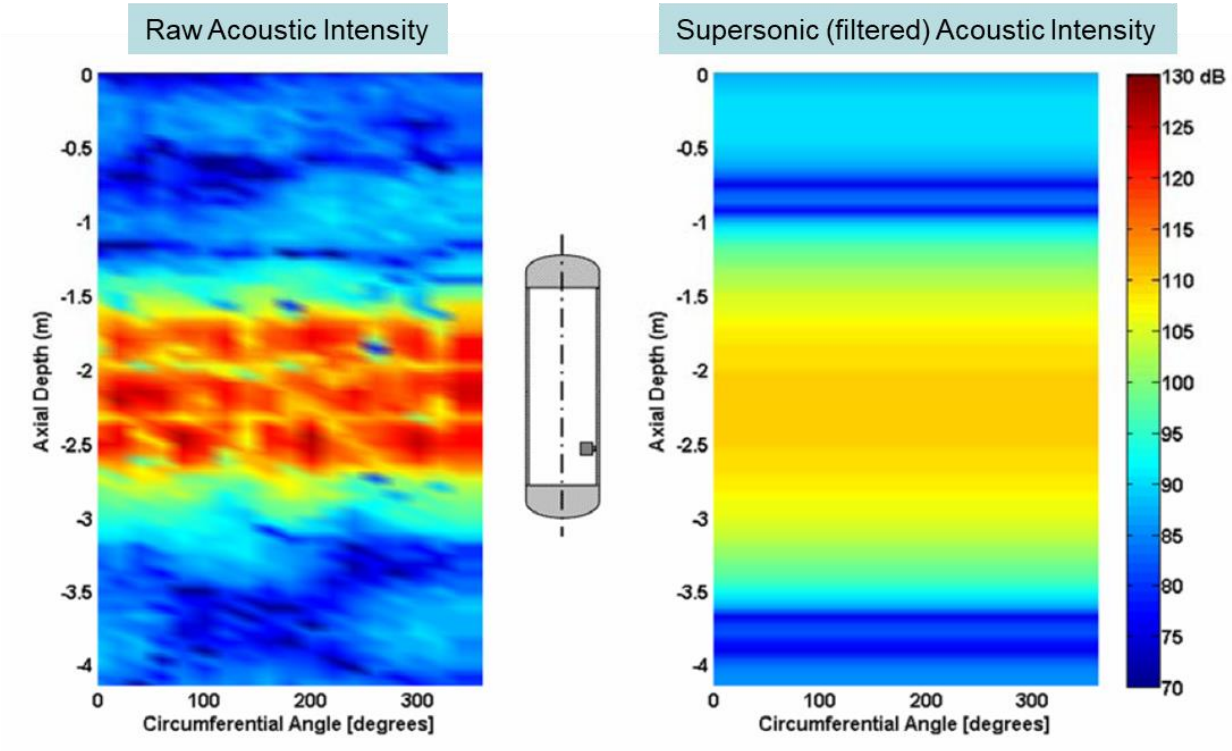

Figure 4: Near-field acoustic intensity near the ($m = 3$, $n = 2$) resonance frequency measured around a cylindrical shell attached to solid hemispherical end caps. The shell spans depths between -2.75 and -1.4 meters. The shell was air-filled and driven transversely with a shaker mounted to a point at a depth of -2.5 m. Left: raw acoustic intensity; Right: filtered supersonic ($k < k_0$) intensity.

[4] This technique is commonly used for Nearfield Acoustic Holography (NAH) applications.

2.2. Statistical Radiation Efficiency

Many shell structures are quite large and have a high *modal density*. In these cases it's common to estimate sound power radiation P_{rad} from an averaged surface vibration $\langle v^2 \rangle$ and the modally-averaged radiation efficiency σ_{rad}. You can learn more about radiation efficiency in my other tutorials [6, 7], but I'll repeat the definition here:

$$\sigma_{rad} = \frac{P_{rad}}{\rho_0 c_0 A \langle v^2 \rangle}$$

where A is the surface area. Szechenyi [8] and the European Space Agency [9] provide empirical formulae for the radiation efficiency given a shell's radius, length, wall thickness, and material properties. Both are based on ratios of frequency over ring frequency, and frequency over critical frequency. Examples of statistically-averaged radiation efficiencies for an 18" diameter 4' long Schedule 40 steel cylindrical shell are compared for both formulae in Figure 5. This example shows how radiation efficiency curves can have two peaks when the ring frequency is lower than the coincidence frequency. As always, however, radiation efficiency above coincidence converges to unity.

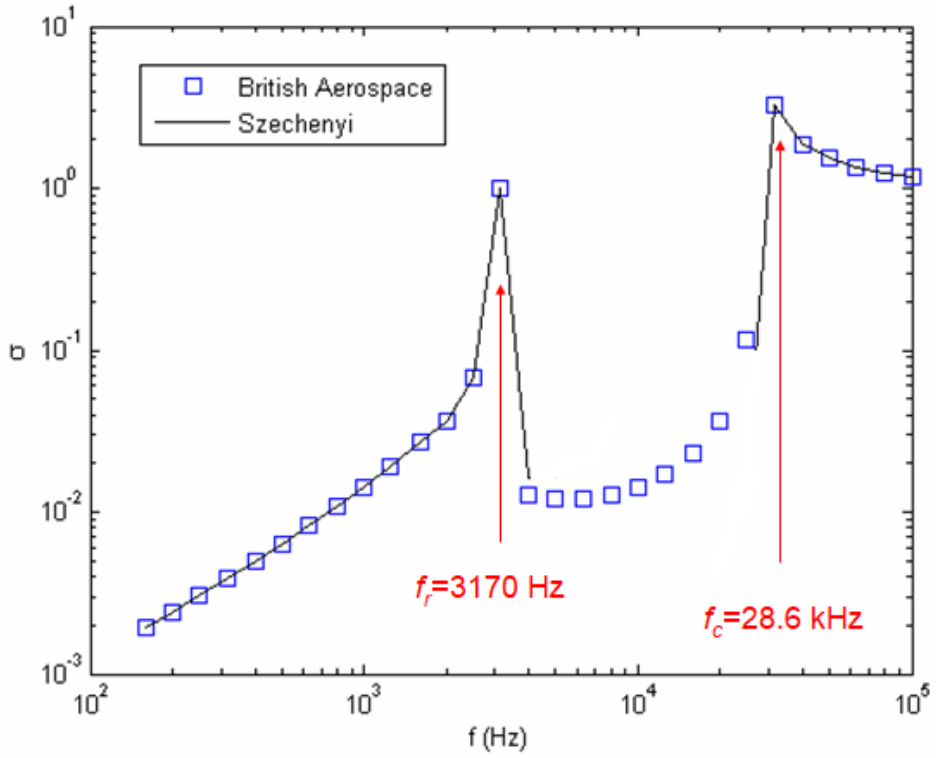

Figure 5: Statistical estimates of averaged radiation efficiency for an 18" diameter Schedule 40 (h ~ 3/8"), 4' long steel cylindrical shell in water using Szechenyi's and the British Aerospace formulations. Efficiency peaks are evident near the ring and coincidence frequencies.

3. INTERIOR SOUND RADIATION

3.1. Low-Frequency Acoustic Plane Wave Behavior

Sound radiated from shells into interior acoustic spaces is extremely complicated, except for the low-frequency case where the acoustic wavelengths are much longer than the shell diameter. In these conditions, the only direction of sound propagation is along the axis of the shell, or the longitudinal direction. The sound waves are often referred to as *plane waves*, since the radial and circumferential pressure variation is constant over the cross-section.

Figure 6 shows sound pressure measured near the outlet of the elbowed pipe from Figure 2, but this time in air [10]. A small loudspeaker near the pipe inlet excited the acoustic plane wave modes inside the interior air column. The bottom of the figure shows images of the measured pressure distributions within the interior air at the m = 2, 3, and 4 axial plane wave modes. Only six pressure tap locations were available, so the modes are a bit coarse. However, the spatial distributions are clearly visible[5].

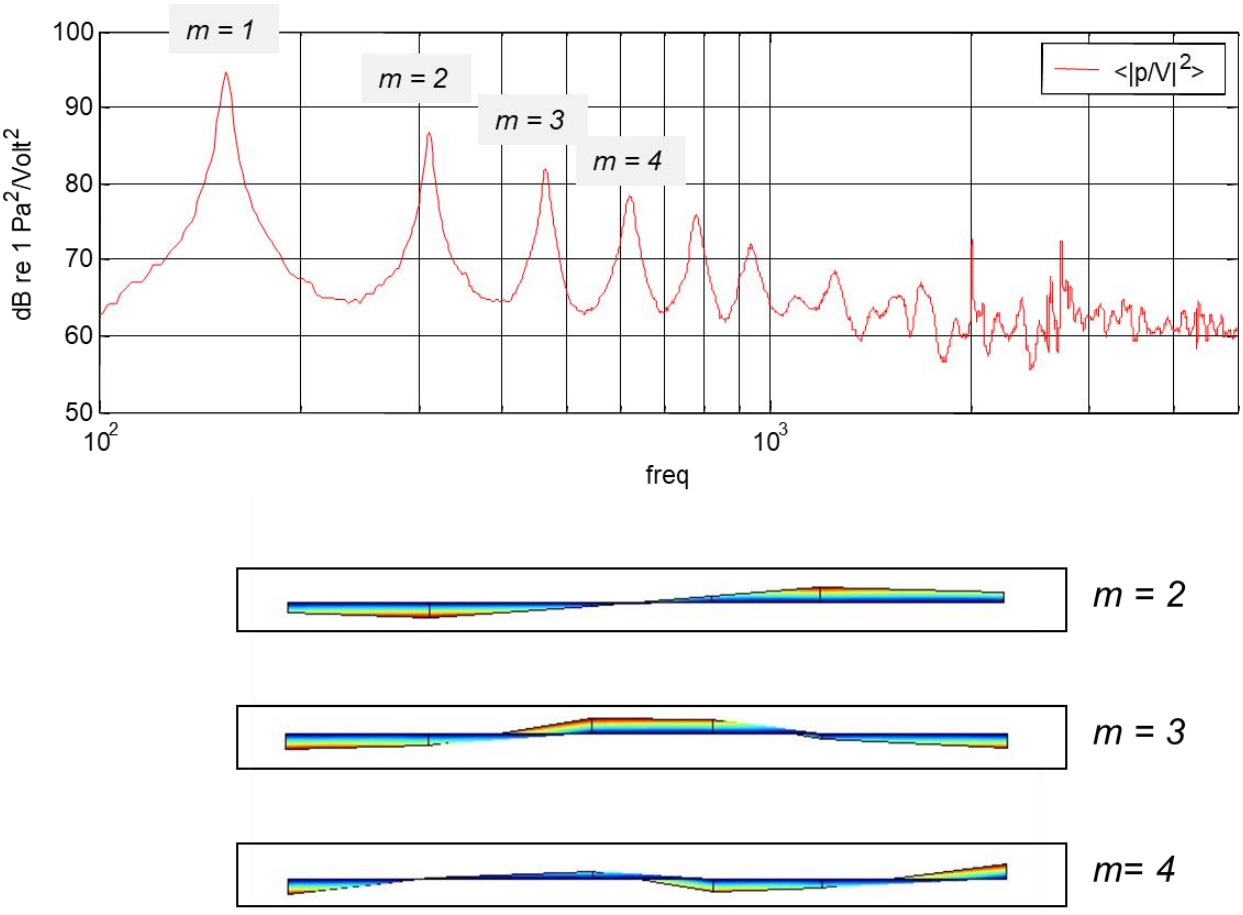

Figure 6: Measured acoustic pressure spectrum within an air-filled elbowed pipe along with spatial distributions of some low-order plane-wave acoustic modes. The pressure spectrum is dominated by plane-wave behavior until a frequency of about 1 kHz, when two- and three-dimensional acoustic modes appear.

[5] The radial direction is used in the acoustic mode shape plots to show relative phase. However, the actual direction of pressure fluctuations is axial.

3.2. Higher Frequency Acoustics

At higher frequencies, the acoustic wavelength shortens until a half wave can be sustained across the pipe diameter. For two-dimensional acoustic waves, like those in channels with flat walls, this frequency is easily calculated as:

$$f_c = \frac{c_0}{2h}$$

where *h* is the channel height. For circular cross-sections, the math is more complicated and involves Bessel functions (which I won't show here). The cut-on frequency is a little lower:

$$f_c = 0.58\frac{c_0}{2a}$$

For the pipe example in Figure 6 (the air-filled case) the cut-on frequency for non-plane wave acoustic modes is about 2 kHz. The pressure frequency response in the plot clearly shifts at that frequency from a simple summation of well-spaced one-dimensional plane wave modes to a higher modal density without strongly defined peaks.

The sound-structure interaction equations for three-dimensional interior acoustics are horrifying. I won't show them here as this is intended to be a simple tutorial. The equations separate the acoustic behavior into longitudinal, radial, and circumferential harmonics. Although the math is difficult, the fundamental coupling between structural modes of vibration and interior acoustic modes is actually quite simple. For strong coupling to occur, two conditions must be met:

- the structural and interior acoustic resonance frequencies coincide (or nearly coincide)
- the structural and interior acoustic mode orders/shapes align (axial and circumferential harmonics)

4. Strong Vibroacoustic Coupling

When the structural and acoustic impedances are comparable, the overall vibro-acoustic response is strongly coupled. Any vibro-acoustic analysis requires a coupled procedure, where the structural normal vibrations into the interior acoustic region are coupled to the normal acoustic pressure gradients within the interior acoustic region.

These equations of motion and coupling procedures require even more detailed mathematics, which is well outside the focus of this tutorial. However, I will explain an important and simple phenomenon: the slowing of low-frequency plane acoustic waves within a flexible walled cylindrical shell. Acoustic plane waves pulsate against the shell walls in-phase around the circumference. This in-phase pressure couples directly with the shell wall hoop strains. After writing equations for the interior pressure and hoop strain and equating the particle velocity and structural normal velocity along the wall surface, an expression for the plane-wave acoustic wave speed within a flexible shell can be derived as:

$$\frac{c_{plane}}{c_0} = \frac{1}{\sqrt{1 + \left(\frac{2a}{h}\right)\left(\frac{\rho_0 c_0^2}{\rho_s c_p^2}\right)}}$$

Note the ratio of the acoustic and structural bulk moduli (ρc^2) in the denominator term, as well as the ratio of shell radius *a* to wall thickness *h*. The higher the structural bulk modulus and wall thickness, the closer the plane wave speed is to the free-space sound speed c_0. Table 1 compares the sound speed ratios for steel and rubber pipe walls. The differences are pronounced, particularly for water.

Table 1: Ratios of plane wave and free-field acoustic sound speeds for various acoustic media and 4” diameter pipes

Acoustic Medium	**Pipe Material**	**Wall Thickness (in)**	c_{plane}/c_0
Air	Steel	¼	1.00
Water	Steel	¼	0.93
Water	Rubber	½	0.01

5. SUMMARY AND CONCLUSIONS

The mathematics which describe the sound-structure interaction between cylindrical shell structures and exterior and interior acoustic spaces is some of the most challenging in the vibro-acoustic field. Here, I have tried to limit the mathematics and instead highlight the key behaviors and parameters which define exterior and interior sound radiation, as well as a strong (but limited) form of vibro-acoustic coupling. I have shown measured and analytic examples to explain those behaviors, including:

- how shell modes with low circumferential order *n* radiate sound, particularly the breathing ($n = 0$), beam ($n = 1$), and ovalling ($n = 2$) modes;
- statistically averaged radiation efficiency curves, which can show two peaks when the ring frequency is lower than the critical frequency;
- interior acoustic fields at low frequencies where the sound is limited to longitudinal plane-wave behavior; and
- how flexible shell walls can reduce the effective sound speed of acoustic plane waves.

6. ACKNOWLEDGEMENTS

I am grateful to:

- Dr. David Feit, who helped me as a young PhD student with the cylindrical shell analytics he and Miguel Junger included in their excellent book [3]. This model was the basis of my Doctoral thesis on minimizing cylindrical shell radiated sound power.
- Ben Doty, a former Penn State MS student who conducted the pipe measurements, both exterior radiated sound power in water and interior acoustic measurements in air.
- Dr. Andrew Barnard, also a former Penn State PhD student, who measured supersonic intensities around a submerged cylindrical shell.

REFERENCES

1. S.A. Hambric. Practical tutorial on cylindrical structure vibro-acoustics part 1 – vibrations. In *Proceedings of Internoise 2022*, Glasgow, Scotland, August 2022.
2. B.J. Doty, et. al. Structural-acoustic measurements of pipes with ninety-degree elbows, under water loading, In *Proceedings of Noise-Con 2005*, Minneapolis, MN, October 2005.
3. M. Junger and D. Feit. *Sound, Structures, and their Interaction*. Acoustical Society of America. 1993.
4. A.R. Barnard, S.A. Hambric, and J.D. Maynard. Underwater measurement of narrowband sound power and directivity using supersonic intensity in reverberant environments. *Journal of Sound and Vibration*, 331, 3931-3944, May 2012.
5. A.R. Barnard and S.A. Hambric, S.A. Design and implementation of a shielded underwater vector sensor for laboratory environments, *Journal of the Acoustical Society of America*, 130 (6), EL387-EL391, December 2011.
6. S.A. Hambric. Structural acoustics tutorial - part 1: Vibrations in structures. *Acoustics Today*, Vol. 2, No. 2, 2006.
7. S.A. Hambric and J.B. Fahnline. Structural acoustics tutorial - part 2: Sound-structure interaction. *Acoustics Today*, Vol. 3, April 2007.
8. E. Szechenyi. Modal densities and radiation efficiencies of unstiffened cylinders using statistical methods. Journal of Sound and Vibration, 19 (1), 65-81, 1971.
9. European Space Agency Structural Acoustics Design Manual (ESA PSS-03-204), 1996.
10. B.J. Doty. *Structural-acoustic measurements of a large, thin-walled cylindrical shell and a small thick-walled pipe with a ninety degree elbow, under water loading*, Penn State MS thesis, 2004.